Nanoscale Advances

ROYAL SOCIETY OF CHEMISTRY

PAPER

View Article Online
View Journal

Cite this: DOI: 10.1039/d5na00930h

Reversible temperature-induced shape transition of Pt nanoparticles supported on Al_2O_3

Ricardo Pool Mazun,†[a] Salman A. Khan,†[bc] Vinson Liao,[b] Thomas W. Hansen,[d] Md Raian Yousuf,[a] Piaoping Yang,[b] Abhijit Shrotri,[e] Adam S. Hoffman,[f] Simon R. Bare,[f] Dionisios G. Vlachos *[b] and Ayman M. Karim *[g]

Received 30th September 2025
Accepted 5th November 2025

DOI: 10.1039/d5na00930h

rsc.li/nanoscale-advances

Supported platinum catalysts are widely used in industry for hydrogenation reactions. The variations of the electronic and geometric properties of Pt nanoparticles due to temperature can greatly affect their reactivity. In this work, we use *in situ* X-ray absorption spectroscopy and environmental transmission electron microscopy to study the effect of H_2 and temperature on the shape and electronic properties of 1.8 nm average diameter Pt nanoparticles supported on Al_2O_3. We utilize actively trained machine learning potentials with uniform acceptance force-bias Monte Carlo (fbMC) to estimate the structural distribution of Pt_{15}/γ-Al_2O_3 (110) clusters at finite temperatures. Our predicted cluster geometries are consistent with experimental data showing the nanoparticles reversibly change shape from 3D hemispheres at low temperatures (35–100 °C) to 2–2.5D rafts at higher temperatures (200–400 °C). Furthermore, experiments and computations indicate that the contraction in Pt–Pt bond distances and higher electron density on Pt at higher temperatures are attributed primarily to the change in nanoparticle shape and associated increased interaction with Al_2O_3. Our results show the fluxional nature of supported Pt nanoparticles driven by temperature changes.

Introduction

Supported metal nanoparticles are widely used in industry as catalysts for different applications including oxidation and hydrogenation reactions[1,2] with previous studies showing a strong particle size and shape effect on reactivity. For example, recent studies of Pt/TiO_2 catalysts for acetylene semi-hydrogenation (from single atoms up to 2.1 nm nanoparticles), furfural decarbonylation/hydrogenation (1.5 to 7.1 nm), and hydrodeoxygenation of furfuryl alcohol (from single atoms up to 5.0 nm) reported significant changes in selectivity, turnover frequencies (TOFs), and apparent activation energies on different Pt nanoparticle sizes.[3–5] For many catalytic studies, the size and shape are typically measured on the initial reduced catalyst. However, supported metal nanoparticles, especially small clusters, are fluxional and dynamic under reactive environments (*e.g.*, the type of adsorbates and their partial pressures) as well as temperature.[6–8] Temperature- or adsorbate-induced changes in size, shape, or electronic properties can have significant consequences on catalytic activity and/or selectivity.[9–12] Therefore, understanding the effect of temperature and adsorbates on the size and shape of metal nanoparticles is of great importance.

Particle size distribution is usually determined by statistical analysis from high-angle annular dark-field scanning transmission electron microscopy images (HAADF-STEM). However, exposure of pretreated samples to air before microscopy can affect the particle sizes and/or shapes. Additionally, supported nanoclusters can present complex gas-dependent metal-support interactions involving both morphological and electronic interactions, as shown by *in situ* high-resolution TEM on Cu/ZnO, Au/CeO_2, and Pt/TiO_2 catalysts.[8,13–18] Another common technique to determine average particle size for supported catalysts is H_2 or CO chemisorption. However, differences between chemisorption and reaction conditions, as well as different size-dependent adsorbate-metal interactions can affect the gas uptake and therefore the estimated particle size. For example, H_2 uptake is typically measured at low temperature compared to reaction, and the quantity of strongly adsorbed H_2 might not be accurate for small nanoparticles and

[a]Department of Chemical Engineering, Virginia Polytechnic Institute and State University, Blacksburg, Virginia 24060, USA

[b]Department of Chemical and Biomolecular Engineering, University of Delaware, Newark, Delaware, 19716, USA. E-mail: vlachos@udel.edu

[c]Department of Chemical Engineering, Indian Institute of Technology Kanpur, Kanpur, Uttar Pradesh, 208016, India

[d]National Centre for Nano Fabrication and Characterization, Technical University of Denmark, DK-2800 Kgs., Lyngby, Denmark

[e]Institute for Catalysis, Hokkaido University, Kita ku, Sapporo, Hokkaido 001-0021, Japan

[f]Stanford Synchrotron Radiation Lightsource, SLAC National Accelerator Laboratory, Menlo Park, California 94025, USA

[g]Department of Chemical Engineering, University of Virginia, Charlottesville, Virginia 22903, USA. E-mail: pqg9zx@virginia.edu

† These authors contributed equally to this work.

clusters.[19,20] In contrast, X-ray absorption fine structure (XAFS) can be performed *in situ* with and without reactive gases and in-*operando* which, complemented by STEM and chemisorption, can be used to determine the effect of the environment on the structure at different temperatures and under reaction conditions. For example, Sanchez *et al.* studied the effect of adsorbates (H_2, CO, O_2 *vs.* He) and temperature on the structure of Pt/C and Pt/Al_2O_3 using XAFS.[21] Their results showed a significant effect of adsorbate and temperature on the Pt electron density, Pt–Pt bond length and disorder. The most significant effect of temperature was the unexpected Pt–Pt contraction of alumina supported 0.9 and 1.1 nm clusters while larger nanoparticles (2.9 nm) showed the expected Pt–Pt expansion at higher temperatures. Other studies also reported this Pt–Pt bond contraction at higher temperatures.[22–24] A later study by Timoshenko *et al.* attributed this Pt–Pt bond contraction to an effect of the lower H_2 coverage and/or the non-Gaussian shape of the bond distribution at higher temperatures.[25] However, in all those studies the shape of the Pt clusters was considered to be unchanged at the different temperatures.

The effect of temperature and adsorbate environments on catalyst structure has also been theoretically studied using first-principles calculations and molecular dynamics (MD) simulations. Sun *et al.*, Mager-Maury *et al.*, and Vila *et al.* studied small alumina supported platinum clusters, ranging from Pt8 to Pt13 using density functional theory (DFT) and MD, and found high fluxionality between 2.5D and 3D structures under varying temperatures and adsorbate environments.[26–28] However, these studies focused on locally optimized clusters and utilized short trajectories of ten picoseconds which cannot efficiently sample the large configurational spaces of supported clusters.[29]

In this work, we studied the effect of temperature and H_2 on the structure of 1.8 nm average diameter Pt nanoparticles supported on γ-Al_2O_3 using X-ray absorption near edge structure (XANES) and extended X-ray absorption fine structure (EXAFS) measurements between 35–400 °C. Our results show that higher temperatures lead to changes in the shape of the nanoparticles and the electron density on Pt, while H_2 mostly affects the electron density of Pt. We further used actively trained machine learning potentials with uniform acceptance force-bias Monte Carlo (fbMC) to estimate the structural distribution of Pt_{15}/γ-Al_2O_3(110) clusters at finite temperatures. Our simulations show cluster contraction and flattening with heating without *a priori* assumptions, consistent with experimental observations. Our results aid in the understanding of structure-sensitive chemistries.

Results and discussion

Pt nanoparticle size and shape at room temperature

The Pt particle size and shape of the reduced 5% Pt/Al_2O_3 catalyst at room temperature were determined using *ex situ* aberration-corrected scanning transmission electron microscopy (STEM) and corroborated with gas chemisorption, and *in situ* EXAFS. Fig. 1a, b, S1 and S2 show representative STEM

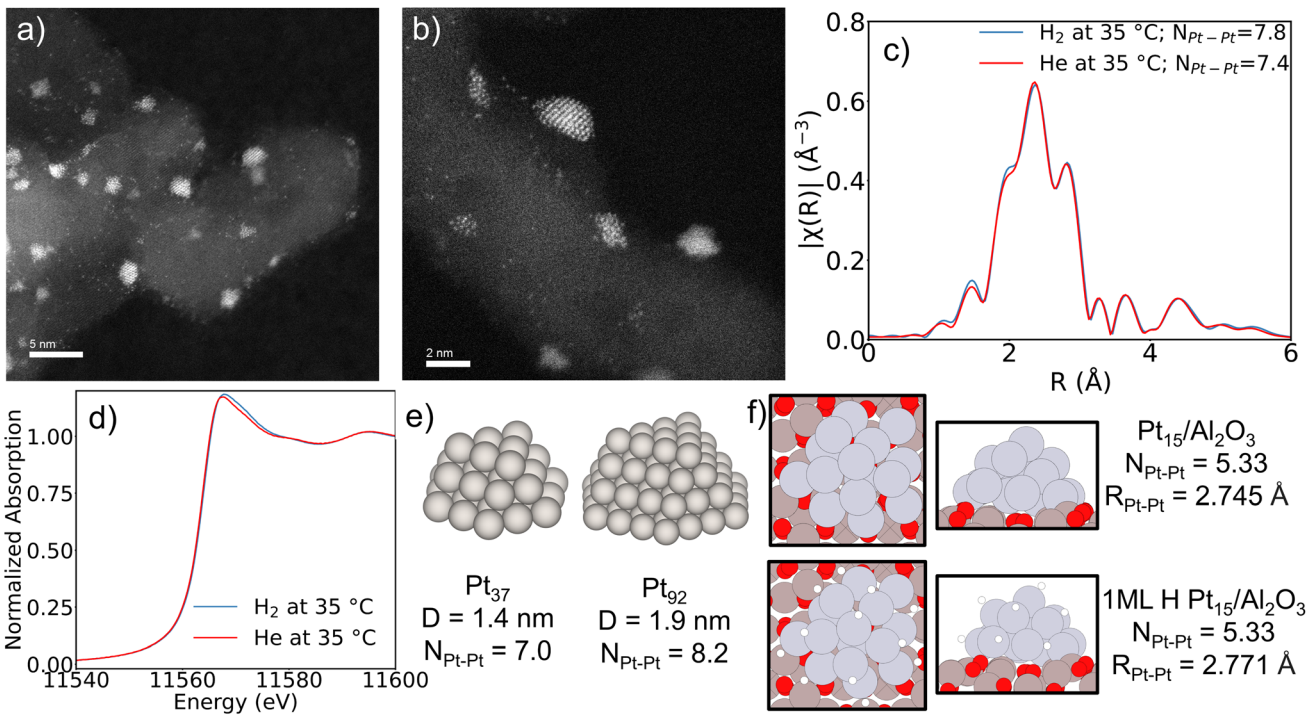

Fig. 1 HAADF-STEM images for 5% Pt/Al_2O_3 after H_2 reduction at 400 °C. (a) Lower magnification, (b) higher magnification image, Pt L_3 EXAFS and XANES spectra of $Pt_{1.8\ nm}$/Al_2O_3 at 35 °C in 50% v/v H_2 and in He (after removal of adsorbed H_2) (c) EXAFS magnitude of the Fourier transformed k^2 -weighted $\chi(k)$ data, $\Delta k = 3–12$ Å^{-1} and (d) XANES. (e) Model hemispherical clusters of varying diameters (D) and their corresponding average first shell coordination numbers (N_{Pt-Pt}). (f) Computed effect of hydrogen adsorption (1 ML) on the shape and bond length of the lowest energy Pt_{15}/Al_2O_3 cluster.

images of the reduced catalyst and the corresponding particle size distribution. The majority of the Pt nanoparticles ranged in diameter from 0.9 to 2.4 nm (see the size distribution in Fig. S2) with a number-average diameter of 1.7 nm and a surface-average (weighted by d^2) diameter of 1.8 nm. Nanoparticles with a hemispherical shape can be seen on the edge of Al_2O_3 in Fig. 1b, S2 and S3. Analysis of multiple nanoparticles showed that the Pt nanoparticle shape is hemispherical (see Fig. S3, Table S1 and associated text for detailed analysis from STEM images), which is common for Al_2O_3 supported catalysts synthesized by impregnation methods.[22,30,31] The total irreversible uptake of CO and H_2 from volumetric chemisorption measurements at 35 °C was 0.55 CO/Pt and 0.52 H/Pt, respectively (Fig. S4). Using a hemispherical shape (based on the results from STEM, and assuming a stoichiometry of 1 : 1 for CO and H to surface Pt atoms, the CO and H_2 chemisorption results are similar and correspond to Pt nanoparticles of ~1.9–2.1 nm in average-surface diameter, which is consistent with the surface-average diameter from STEM. The Pt–Pt coordination number (CN) from model fit of the EXAFS spectra in H_2 and in He at room temperature (Fig. 1c) was 7.8 ± 0.4 and 7.4 ± 0.3, respectively. The fit results are shown in Table S2, Fig. S5 and S6 and a comparison of spectra in He and H_2 is shown in Fig. S7. Comparing the experimental CNs (7.8 ± 0.4 in H_2 and 7.4 ± 0.3 in He) with geometrical models of hemispherical cubooctahedron Pt nanoparticles of different sizes (Fig. 1e, CN of 7.0 for 1.4 nm and 8.2 for 1.9 nm) indicates that the average Pt NP size based on the EXAFS CNs is between 1.4 nm and 1.9 nm which is consistent with the average diameter from other characterizations.

DFT calculations on Pt_{15}/γ-Al_2O_3 (110) show that the hemispherical shape is the most stable at low temperatures in the absence of adsorbates. Pt_{15} was chosen as it was one of the smallest cluster sizes observed in STEM images and it is not feasible to model larger sizes with DFT. Hydrogen adsorption up to 1 monolayer (ML) on Pt_{15} only resulted in elongation of Pt–Pt bonds without a significant change in the overall shape as shown in Fig. 1f and S8, consistent with our EXAFS results (Table S2). Higher H_2 coverage (>1.4 H : Pt) could change the shape of Pt NPs,[27,32] but this requires much higher partial pressures (*e.g.* 10 bar at 183 K)[33] than in our studies (0.5 bar). Our results are consistent with previous work[21,23,28,32,34,35] on Pt/C and Pt/Al_2O_3 where H_2 adsorption at room temperature (and atmospheric pressure) lowers the electron density on Pt, as reflected in the higher white line intensity in Fig. 1d, and elongates the Pt–Pt bonds (see Table S2) but does not significantly affect the shape of the nanoparticle as seen from the small difference in CN (slightly larger in H_2 *vs.* He). The STEM, chemisorption, and EXAFS analysis results at room temperature complemented by theoretical calculations indicate that the Pt/Al_2O_3 consists mostly of hemispherical nanoparticles with an average diameter of 1.8 nm. For the sake of brevity, in the following discussions, the catalyst will be represented by the average diameter of the Pt NPs and referred to as $Pt_{1.8\ nm}/Al_2O_3$.

Effect of temperature on the structure of $Pt_{1.8\ nm}/Al_2O_3$

The effect of temperature on the structure of $Pt_{1.8\ nm}$ nanoparticles was investigated using *in situ* EXAFS and corroborated with first-principles calculations and environmental transmission electron microscopy (ETEM). The EXAFS spectra in Fig. 2a and b show a reduction of the scattering amplitude and an apparent shortening of Pt–Pt bonds at higher temperatures. As the temperature increases, the decrease in scattering amplitude is due to the significant dampening of the EXAFS oscillations at both low and high k values as seen in Fig. 2c. Thermal disorder dampens the EXAFS oscillations at all k values

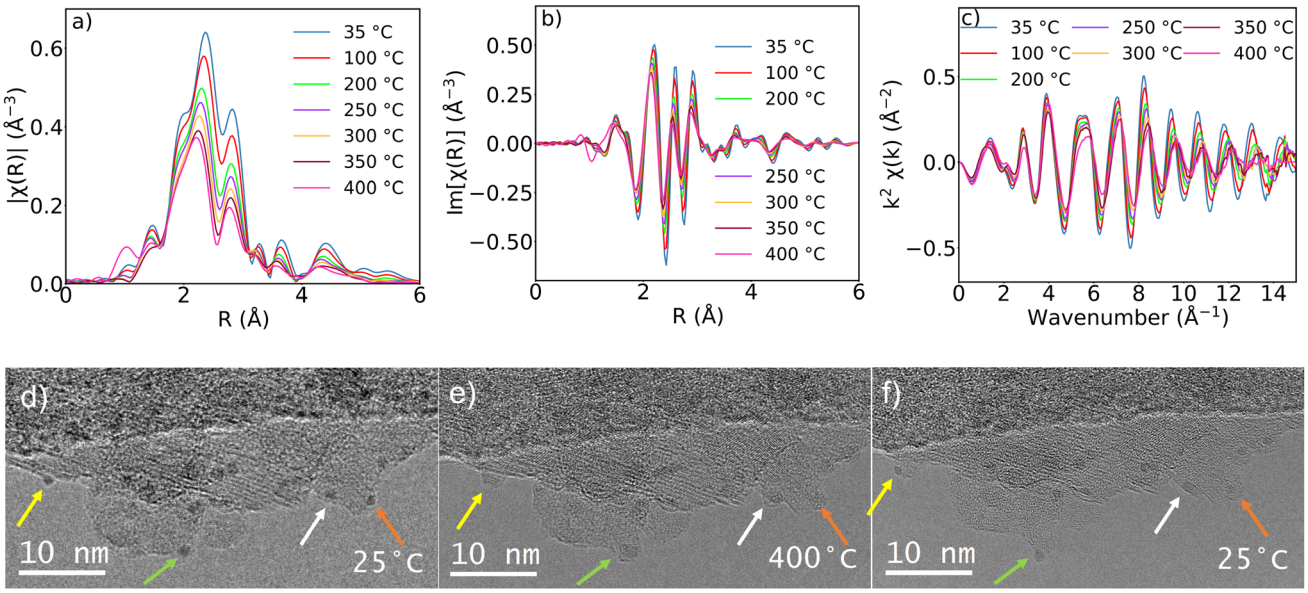

Fig. 2 Pt L_3 EXAFS spectra of $Pt_{1.8\ nm}/Al_2O_3$ at different temperatures in 50% v/v H_2 (a) magnitude and (b) imaginary parts of the Fourier-transformed k^2-weighted $\chi(k)$ data in (c) ($\Delta k = 3$–12 Å^{-1}). ETEM images of $Pt_{1.8\ nm}/Al_2O_3$ at low (25 °C) and high (400 °C) temperatures in vacuum (d–f). The colored arrows point to the same nanoparticles at 25 and 400 °C to highlight the reversible structural changes.

but its effect is stronger at high k values. However, the concomitant dampening in EXAFS oscillations at lower k values indicates that a second contributing factor is likely responsible for the reduction in scattering amplitude seen in Fig. 2a at higher temperatures. Such a reduction in the EXAFS oscillations at all k values is typically observed for nanoparticles of different sizes or shapes, or more specifically, nanoparticles with different average Pt–Pt coordination (see simulations for effect of coordination number *vs.* disorder and comparisons with EXAFS on smaller NPs in Fig. S9 and S10). To provide more insights into the temperature-induced structural changes, the EXAFS data in Fig. 2c was fitted and the fit details are presented in Tables S2, S3, Fig. 3, S5, S6 and S11–13. The results in Fig. 3 show that in addition to the increased disorder and the contraction of Pt–Pt bonds as the temperature increased from 35 to 400 °C, the average Pt–Pt coordination decreased from 7.8 ± 0.4 to 6.2 ± 0.4. This decrease in the average Pt–Pt coordination is significant and is well outside of the fit uncertainty. We note that the structural changes were reversible as the temperature decreased to 35 °C at the end of the experiment (see Fig. S14). While disintegration of the nanoparticles would also lead to a decrease in the Pt–Pt CN, this disintegration of Pt nanoparticles has only been reported in oxygen at much higher temperatures and was also irreversible unless the gas atmosphere was changed to reducing conditions.[36,37] The contraction in Pt–Pt bond distance and decrease in Pt–Pt CN were observed at 400 °C compared to 35 °C in both H_2 and He (Fig. 2a–c, S15, Tables S2 and S3) indicating that temperature is mainly responsible for the observed structural changes of the 1.8 nm Pt nanoparticles, rather than temperature-dependent H_2 coverage and will be further discussed below (Fig. S15 shows the effect of increasing temperature on EXAFS and XANES in He).

Before discussing the EXAFS results in more detail, it is important to note the similarities and the differences between our work and previous studies. Our Pt/Al_2O_3 catalyst consists of hemispherical shaped nanoparticles with an average diameter of ~1.8 nm and average first shell CN of 7.8. This size and average CN are intermediate in the range of previously reported transition from negative (CN < ~9.0) to positive thermal expansion (CN > ~9.0).[23,24] Additionally, for a similar size, Pt nanoparticles with an initial 3D shape at low temperature were reported to have positive thermal expansion while those that wet the Al_2O_3 support (hemispherical or more disk-shaped) showed negative thermal expansion similar to our work.[24] However, most of the previous studies were conducted under H_2 with only a few experiments performed in He or vacuum. It is well known that H_2 adsorption causes an overall relaxation of the Pt nanoparticles and subsequent elongation of Pt–Pt bonds.[21,23,28,32,34,35] Therefore, a shorter Pt–Pt bond distance at higher temperatures could be due to lower coverage of H adsorbed on the surface of the nanoparticles. Our results show that the contraction of Pt–Pt bond distance at higher temperatures was observed in both H_2 and in He, *i.e.* in the absence of chemisorbed H (Fig. S15, Tables S2 and S3) and therefore cannot be attributed solely to the decrease in H_2 coverage. In addition to the shortening of the Pt–Pt bonds at higher temperatures, we observed a significant decrease in the Pt–Pt CN from 7.8 and 7.4 at 35 °C to 6.2 and 5.8 at 400 °C in H_2 and He, respectively. Sanchez *et al.* also observed a decrease in the Pt–Pt CN of 0.9 and 1.1 nm clusters supported on Al_2O_3 at higher temperatures.[21] Specifically, for the 0.9 nm clusters in He, the average first shell Pt–Pt CN decreased from ~5.9 at −107 °C to ~5.0 at 300 °C.[21] However, they considered the difference to be too small to determine a change in the cluster structure/shape. Other studies considered the CN, and consequently the size/shape, to be unchanged/constant at different temperatures.[23–25,33] Clearly, the size and shape of the nanoparticles, interface with the support, and the identity of the support are all important factors in determining the effect of temperature on the structure of the Pt nanoparticles. We believe that the observed decrease in CN which has been mostly overlooked in previous studies, and the associated decrease in Pt–Pt bond distances are related, and arise from a temperature-induced shape change which is discussed next.

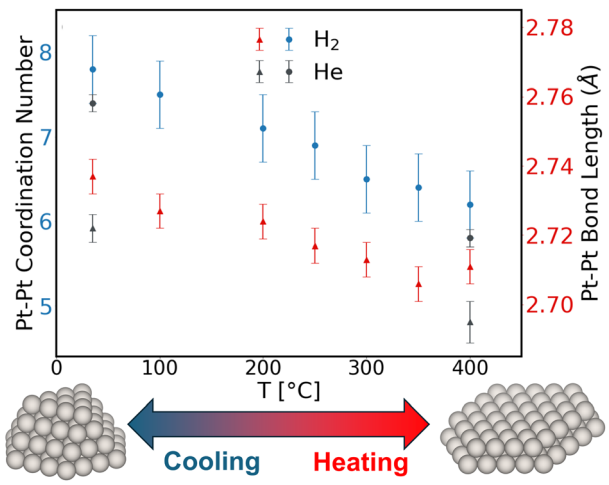

Fig. 3 Average Pt–Pt coordination number and Pt–Pt bond length (Å) under a 50% v/v H_2 and pure He between 35–400 °C. The geometrical models indicate nanoparticle shapes consistent with the coordination numbers.

First, we discuss the observed decrease in Pt–Pt CN at higher temperatures, possible analysis artifacts and the most plausible structural interpretation. We note that the size distribution, the disorder of nanoparticles and the further increase of the disorder with an increase in temperature can influence the CNs extracted from EXAFS. The increase in disorder can lead to deviation from Gaussian distribution of the bond lengths that is typically assumed in analysis of the EXAFS spectra. While the deviation from a Gaussian bond length distribution can lead to significantly shorter bond lengths from the traditional EXAFS analysis,[38] the effect is less pronounced on CN.[39,40] For example, the effect of the non-Gaussian bond length distribution on the first shell CNs of 1.6 nm Pt nanoparticles was small (~5% error in CN) based on EXAFS fits of spectra calculated from molecular dynamics trajectories at different temperatures.[40] Similar results were obtained from EXAFS fits of molecular dynamics simulations of Au_{147} nanoparticles where the error between the CN from EXAFS was within 7% of the actual CN.[41] Only when the

disorder was extremely large due to the presence of strongly binding ligands (thiols onAu_{147}, ${\sigma_{Au-Au}}^2 = 0.0268$ Å^2), the CN was underestimated by ~30%.[41] The disorder obtained from our EXAFS analysis at 400 °C, ${\sigma_{Pt-Pt}}^2 = 0.013$ Å^2, is low compared to the cases reported in the literature where the CNs were underestimated. Therefore, we do not expect a significant effect of the increased disorder at higher temperatures on the CNs extracted from EXAFS.

Since the temperature-induced changes are reversible (see EXAFS in Fig. S14 and also ETEM in Fig. 2d–f and S22), we can rule out a significant change in the size of the Pt nanoparticles (or more accurately the total number of Pt atoms per nanoparticle) throughout the heating and cooling cycles. It is well known that, for the same number of atoms in the nanoparticle, changes in nanoparticle structure/shape can have a significant effect on the Pt–Pt CNs.[23,32,41–43] Fig. S16–S20 show geometric models of nanoparticles of different shapes with a constant number of atoms and their corresponding average Pt–Pt CN. The average Pt–Pt CN decreases as the shape flattens from a hemispherical geometry. Therefore, based on the reversibility of the observed changes in CN and the effect of shape on CN for the same number of atoms in the NP shown in Fig. S16, the results strongly suggest that as the temperature increases the Pt nanoparticles change shape from a hemispherical to a flatter structure as shown by the geometrical models in Fig. 3.

To corroborate the EXAFS observations of reversible flattening of Pt NPs at elevated temperatures, ETEM experiments were conducted to monitor the shape of the Pt nanoparticles at low and high temperatures. The experiments were conducted at a base pressure of around 10^{-7} mbar. A reasonably flat area of the Al_2O_3 support was located and the size and shape of the particles were determined. Fig. 2d shows several Pt NPs in the size range from 0.9–1.6 nm, and similar to the STEM results in Fig. 1, the NPs are mostly hemispherical. After the initial image acquisition, the beam was blanked leaving the sample unexposed to the electron beam. The temperature was increased to 400 °C at a rate of ~10 °C min^{-1} and a new set of images were acquired. At 25 °C (Fig. 2d and f), the NPs on the edge of the support appeared hemispherical, wetting the substrate only slightly. As the temperature increased (Fig. 2e), the Pt NPs increasingly wetted the substrate. The flattening at 400 °C can be especially seen for the NPs highlighted by yellow and green arrows in Fig. 2e where the projection of the NPs increases in area (see Fig. S21) at 400 °C compared to 25 °C. This observation agrees with the interpretation of the decreasing CN measured by EXAFS at increasing temperatures. Furthermore, several heating/cooling cycles were performed and the nanoparticles switched between hemispherical at 25 °C (Fig. 2d, f, S22a, c and e) and flat at 400 °C (Fig. S22b and d) confirming the reversibility of the shape change observed from our EXAFS results. The reversibility of the temperature-induced structural change observed by EXAFS and ETEM indicates that the Pt nanoparticles adapt their structure to changes in the local chemical environment, the adsorption/desorption of H_2, and more strongly to the increase in temperature, highlighting their fluxionality.

The shortening of Pt–Pt bonds with increasing temperature has been reported previously for different Pt cluster sizes and shapes supported on Al_2O_3.[21,23,24] However, as discussed earlier, this is more complex to interpret because the increase of the disorder at higher temperatures could lead to deviation from Gaussian distribution of the bond lengths that is typically assumed in analysis of the EXAFS spectra and consequently could result in significantly shorter bond lengths from the EXAFS fits.[38] A quasi-harmonic approximation (the method used in our work) introduces the third cumulant to account for the effect of skewness of the bond distribution on the average Pt–Pt bond distance extracted from EXAFS.[38] The quasi-harmonic approach has been shown to be effective in accurate extraction of the average bond distance (within 0.01 Å) even for highly disordered Au_{147} with thiol ligands on the surface.[41] However, a recent study by Timoshenko *et al.* questioned the validity of the cumulant approach and developed a neural network method to further improve the EXAFS analysis of disordered materials with non-Gaussian bond length distributions.[25] Their neural network analysis showed different results compared to the quasi-harmonic approximation using the third cumulant. Specifically, the previously reported negative thermal expansion obtained using the quasi-harmonic approximation on Pt/Al_2O_3 samples[24] was less pronounced or the trend was reversed to a positive expansion. However, in contrast to the quasi-harmonic approximation results showing positive thermal expansion for the Pt foil, the neural network analysis of the Pt foil showed a decrease in Pt–Pt bond distance with increase in temperature from −107 to 200 °C before increasing at 400 °C,[25] highlighting the challenge in the detailed analysis of even a bulk ordered material.

Our EXAFS analysis uses the quasi-harmonic approximation to account for the higher disorder and deviation from Gaussian distribution of Pt bond lengths at higher temperatures. Furthermore, to provide more evidence, we analyzed the more distant Pt scattering shells (up to the fourth) since the disorder has a smaller effect on the average bond distance for more distant shells.[44] The fit results (Tables S4–S6 and Fig. S23–28) showed a decrease in the CNs for all scattering paths and also showed a contraction in Pt–Pt distances for most of the scattering paths in the more distant shells. Given that the NPs do change shape, it is not clear how the Pt–Pt distances would be expected to change beyond the first Pt–Pt shell. Nevertheless, our results indicate that both the Pt–Pt CN and bond distance decrease as the temperature increases.

Next, we investigated the effect of temperature on Pt_{15}/Al_2O_3 cluster structure with uniform acceptance force-bias Monte Carlo (fbMC), an enhanced sampling method that provides large accelerations over unbiased Monte Carlo and molecular dynamics (see Methods for details).[45] fbMC simulations were performed from 25 °C to 425 °C at 100 °C intervals. Each simulation was initialized with the lowest energy Pt_{15}/Al_2O_3 isomer (which is hemispherical in shape) and was run for a total of 50 million fbMC steps, which is estimated to sample a timescale in the order of 500 ns.

From 25 °C to 325 °C, the cluster remains 3D during the course of the simulation while at 425 °C it transitions from 3D

to 2D. The 3D to 2D transition at elevated temperatures can be attributed to the enhanced mobility of the cluster. The cluster samples the configurational space more effectively and readily overcomes energy barriers leading to the 3D to 2D transition. Fig. 4a and b show the probability density functions (pdfs) of Pt–Pt CN (N_{Pt-Pt}) and Pt–Pt bond lengths (R_{Pt-Pt}) at 25 °C and 425 °C, with the distribution means shown in the legends. The Pt–Pt pair distribution functions (normalized by the volumes of the shells) at both temperatures are shown in Fig. S29. Fig. 4c and d show snapshots of a 3D Pt_{15} cluster at 25 °C and a flat Pt_{15} cluster at 425 °C, respectively. The CN pdf shifts to lower CN values at 425 °C as lower CN Pt_{15} clusters become thermodynamically accessible. With this associated CN change, the distribution of Pt–Pt bond lengths also shifts to lower bond length values. Fig. 4b shows the decrease in the mean R_{Pt-Pt} from 2.78 Å to 2.67 Å. This decrease is attributed to contributions from both the nearest neighbor and the 2nd nearest neighbor shells. The shift in the nearest neighbor peak from 2.62 Å to 2.59 Å is shown in Fig. 4b (dashed lines) as the cluster transitions to a flat configuration. Furthermore, the second nearest neighbor shell around 3.3 Å vanishes as the cluster transitions to a flat configuration at 425 °C. To further elucidate how changes in CN and Pt–Pt bond length correlate with shape change, Fig. S30 shows correlations between N_{Pt-Pt}, R_{Pt-Pt}, and the cluster center of mass (CoM) height (Z_{CoM}) using data aggregated from all five temperatures. Higher Z_{CoM} values correspond to hemispherical clusters, while smaller Z_{CoM} values correspond to flat clusters. Our simulations demonstrate that flat Pt_{15} configurations are correlated with lower CNs and shorter Pt–Pt bond distances, while hemispherical Pt_{15} configurations are correlated with higher CNs and longer Pt–Pt bond distances.

In summary, our fbMC simulations support the experimentally observed flattening of Pt_{15}/Al_2O_3 clusters at higher temperatures and qualitatively reproduce the positive correlation between Pt–Pt bond length and CN with temperature as observed with EXAFS. The shorter Pt–Pt distances and change in shape to flatter structures (larger interfacial area) at higher temperatures are expected to have a significant effect on the extent of charge transfer between Pt and Al_2O_3 which is discussed next.

Temperature induced electronic effects on platinum

A significant effect of temperature on the electronic properties of platinum was observed through XANES as seen from the decrease in the white line intensity and shift of the edge to lower energy as the temperature increased in He and H_2 as shown in Fig. 5a and S31, respectively. We note that the experiment was designed to check for reversibility (Fig. S14) of the structure and electronic properties in H_2 and He, *i.e.* after complete desorption of H_2 as explained in the methods section. The decrease in the white line intensity of Al_2O_3 supported Pt NPs at higher temperatures in the presence of H_2 has been previously reported in literature but was solely attributed to a decrease in H_2 coverage, as a constant Pt nanoparticle shape was assumed.[33] However, our results also show the decrease in white line intensity at higher temperatures in He (Fig. 5a). Additionally, our EXAFS results, supported by ETEM and fbMC simulations, clearly show that higher temperatures induce significant structural changes, leading to flattening of the NPs. While H_2 adsorption affects the electronic properties and structure of the NPs as discussed above, our results indicate that the significant structural and electronic changes are mostly induced by temperature, and not by temperature-dependent H_2 coverage on the Pt nanoparticles. Therefore, using the changes in XANES to estimate coverage of different adsorbates should be used with caution, and possibly only over a small temperature range where the structure/shape of the NPs stays mostly unchanged.

We hypothesize that the observed decrease in the white line intensity (and thus increased electron density on Pt) as temperature increases is due to additional wetting with the support as the Pt NPs change shape from 3D hemispheres to 2–2.5D rafts as shown in Fig. 2d, e, 3, and 4, where 2–2.5D refers to the number of layers being 1 or larger, but less than the number

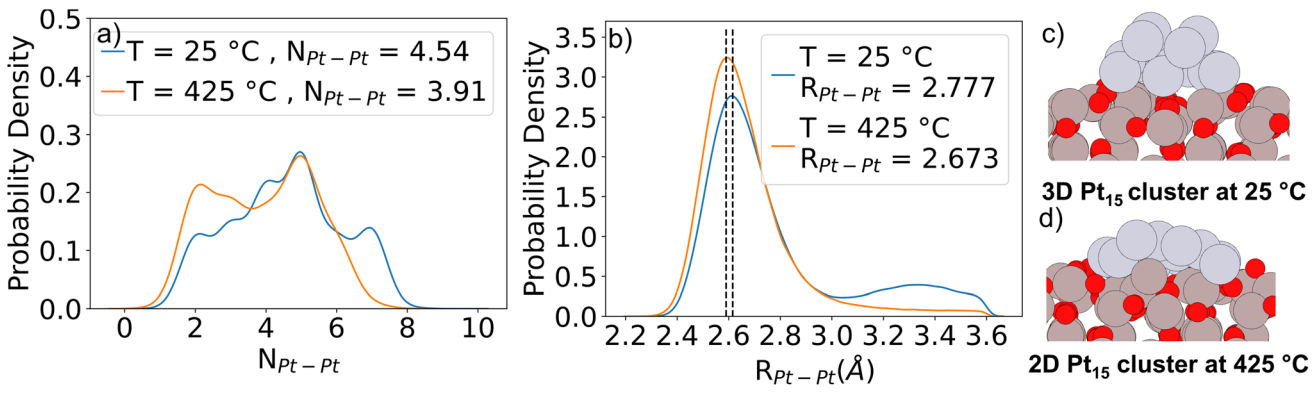

Fig. 4 Geometric statistics and trajectory snapshots of Pt_{15}/Al_2O_3 sampled *via* fbMC at 25 °C and 425 °C. (a and b) Predicted probability distributions for coordination number (N_{Pt-Pt}) and Pt–Pt bond length fit *via* kernel density estimation, respectively. As temperature increases, the coordination number distribution becomes broader towards lower values of N_{Pt-Pt}, suggesting that undercoordinated structures become more accessible upon heating. A decrease in average N_{Pt-Pt} is accompanied by an associated decrease in average Pt–Pt bond length. (c) Snapshot of a 3D configuration at 25 °C. (d) Snapshot of a configuration after the Pt cluster transitions to 2D at 425 °C.

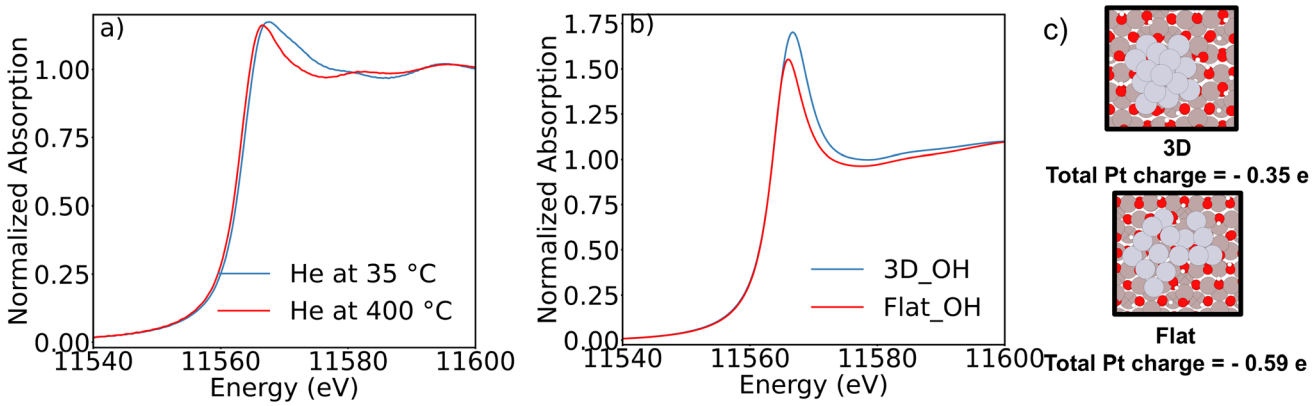

Fig. 5 Pt L_3 XANES for $Pt_{1.8\ nm}/Al_2O_3$ at 35 °C and 400 °C in (a) He. (b) Calculated Pt L_3 XANES for hemispherical and flat Pt clusters on hydroxylated Al_2O_3. (c) Hemispherical (top) and flat (bottom) clusters on hydroxylated Al_2O_3 with total Pt charges.

of layers in a hemispherical NP. The calculated net atomic charge transfer from the support to the cluster for an ensemble of Pt_{15}/Al_2O_3 isomers as a function of average Pt CN is shown in Fig. S32. For all cluster shapes studied, the cluster gains anywhere from −0.4 to −1.2 eV of charge, but an obvious correlation between net electron density and CN does not exist. However, we note that due to the extreme hydrophilicity of γ-alumina and the difficulty in complete dehydroxylation of the surface even in He at 400 °C, a nonzero coverage of hydroxyl groups is expected.[46] Therefore, we performed an analogous study on flat and hemispherical NPs and added 11.8 OH nm^{-2} of hydroxyl coverage to the support (Fig. 5c). The support was hydroxylated in the most stable positions as reported in literature[46] and subsequently relaxed in DFT. We perform this study at constant hydroxyl coverage despite differing temperatures as the sample is exposed He at 400 °C to desorb all the H_2 then cooled down in He to 35 °C. Therefore, the hydroxyl density in He is expected to remain constant at both temperatures. For these calculations, we selected two pairs of flat and hemispherical NPs studied in Fig. S32, where for one pair the electron density is higher on the flat NP and for the other pair the electron density on the hemispherical NP was higher than the flat NP. We notice from the results in Fig. S33 and 34 that the addition of hydroxyl groups (1) decreases the net electron density on the clusters compared to the dry surface and (2) the electron density on the flat clusters decreases to a lesser extent compared to the hemispherical clusters. Therefore, adding hydroxyl groups appears to increase the difference in electron density between the flat and hemispherical clusters in favor of more e− on the flat ones, as shown in Fig. 5c, S33 and S34. To qualitatively correlate these results with experiments, we performed Pt L_3 XANES simulations on the flat and hemispherical Pt_{15} NPs on dry and hydroxylated Al_2O_3. The calculated XANES spectra on the pair of clusters where the flat cluster had a higher electron density show a significantly lower white line intensity on the flat Pt_{15} NP compared to the 3D shape on the hydroxylated Al_2O_3 (Fig. 5b) while the difference was smaller on the dry Pt_{15}/Al_2O_3 (Fig. S35). Additionally, for the second pair of clusters where the flat cluster has lower electron density, the white line intensity for the flat cluster was still slightly lower than that for the hemispherical 3D cluster on the hydroxylated surface (Fig. S36a and b) and to a lesser extent on the dry surface (Fig. S36c and d). We note that while the results are in qualitative agreement with the experimental results, the XANES simulations were performed on a much smaller cluster (Pt_{15}) than the average size from experiments and therefore, the results should not be quantitatively compared. Additionally, the XANES simulations on dry and hydroxylated Al_2O_3 indicate that the lower white line intensity from XANES on Pt is a complex function of size/shape and electron density as previously reported,[47] as well as the interaction with OH^- and Al_2O_3. Therefore, further investigation is needed to deconvolute these effects and is the scope of future work.

Conclusions

In this work, we studied the effect of temperature and H_2 on the structure of Al_2O_3-supported 1.8 nm Pt nanoparticles using XANES, EXAFS and ETEM, and identified a dependence of particle shape on temperature. As temperature increases, the clusters transition from hemispherical in shape to flatter 2–2.5D rafts irrespective of the chemical environment (He or H_2). Additionally, the shape change is accompanied by an increase in Pt electron density. Our results are corroborated using DFT calculations and force-bias Monte Carlo (fbMC) simulations of a Pt_{15}/γ-$Al_2O_3(110)$ model system. The fbMC simulations predict cluster flattening and Pt–Pt bond contraction at elevated temperatures while DFT shows increased interactions of flat Pt clusters with hydroxyl groups on Al_2O_3 leading to higher electron density on Pt. Our results demonstrate the fluxional nature of nanocatalysts and are important in aiding the understanding of structure-sensitive chemistries.

Author contributions

AMK and DGV conceptualized the project. RPM and AMK designed all the experiments. SAK and DGV designed the theoretical work. RPM synthesized and characterized the

catalyst and performed experimental data analysis. MRY performed the EXAFS experiments in collaboration with ASH and SRB at SSRL and performed H_2 and CO chemisorption. AMK performed all EXAFS model fits and analyses. AS conducted AC-STEM and TWH conducted ETEM. SAK performed the fbMC simulations and analysis. VL performed the DFT calculations and analysis. PY performed the XANES simulations and analysis.

Conflicts of interest

The authors declare no conflict of interest.

Data availability

The data supporting this article can be obtained upon request by contacting Ayman M. Karim at pqg9zx@virginia.edu (for experimental data) and Dionisios G. Vlachos at vlachos@udel.edu (for computational data).

Supplementary information is available. See DOI: **https://doi.org/10.1039/d5na00930h**.

Acknowledgements

This research was supported by the U.S. Department of Energy, Office of Science, Office of Basic Energy Sciences, Catalysis Science program, under award DE-SC0022144. This research was supported in part through the use of Information Technologies (IT) resources at the University of Delaware, specifically the high-performance computing resources. The microscopy work was supported by the Cooperative Research Program of Institute for Catalysis, Hokkaido University (20A1004 and 22DS0123). Use of the Stanford Synchrotron Radiation Light Source (SSRL, beamline 9–3, user proposal 4645), SLAC National Accelerator Laboratory is supported by the U.S. Department of Energy, office of Basic Energy Sciences under Contract No. DE-AC02-76SF00515. Additional support by the Consortium for *Operando* and Advanced Catalyst Characterization *via* Electronic Spectroscopy and Structure (Co-ACCESS) at SLAC is acknowledged. Co-ACCESS, is supported by the U.S. Department of Energy, Office of Science, Office of Basic Energy Sciences, Chemical Sciences, Geosciences and Biosciences under Contract DE-AC02-76SF00515. Finally, we thank Dr Fernando Vila for insightful discussions and feedback.

Notes and references

1 I. Chorkendorff and J. W. Niemantsverdriet, *Concepts of Modern Catalysis and Kinetics*, John Wiley & Sons, 2017.
2 L. Zhang, M. Zhou, A. Wang and T. Zhang, *Chem. Rev.*, 2019, **120**, 683–733.
3 C.-T. Kuo, Y. Lu, L. Kovarik, M. Engelhard and A. M. Karim, *ACS Catal.*, 2019, **9**, 11030–11041.
4 V. V. Pushkarev, N. Musselwhite, K. An, S. Alayoglu and G. A. Somorjai, *Nano Lett.*, 2012, **12**, 5196–5201.
5 J. Fu, J. Lym, W. Zheng, K. Alexopoulos, A. V. Mironenko, N. Li, J. A. Boscoboinik, D. Su, R. T. Weber and D. G. Vlachos, *Nat. Catal.*, 2020, **3**, 446–453.
6 P. Nolte, A. Stierle, N. Jin-Phillipp, N. Kasper, T. Schulli and H. Dosch, *Science*, 2008, **321**, 1654–1658.
7 F. Tao, S. Dag, L.-W. Wang, Z. Liu, D. R. Butcher, H. Bluhm, M. Salmeron and G. A. Somorjai, *Science*, 2010, **327**, 850–853.
8 P. L. Hansen, J. B. Wagner, S. Helveg, J. R. Rostrup-Nielsen, B. S. Clausen and H. Topsøe, *Science*, 2002, **295**, 2053–2055.
9 M. J. Kale and P. Christopher, *ACS Catal.*, 2016, **6**, 5599–5609.
10 N. C. Nelson, L. Chen, D. Meira, L. Kovarik and J. Szanyi, *Angew. Chem., Int. Ed.*, 2020, **132**, 17810–17816.
11 M. E. Grass, Y. Zhang, D. R. Butcher, J. Y. Park, Y. Li, H. Bluhm, K. M. Bratlie, T. Zhang and G. A. Somorjai, *Angew. Chem., Int. Ed.*, 2008, **47**, 8893–8896.
12 J. C. Matsubu, V. N. Yang and P. Christopher, *J. Am. Chem. Soc.*, 2015, **137**, 3076–3084.
13 J. B. Wagner, P. L. Hansen, A. M. Molenbroek, H. Topsøe, B. S. Clausen and S. Helveg, *J. Phys. Chem. B*, 2003, **107**, 7753–7758.
14 S. Helveg and P. L. Hansen, *Catal. Today*, 2006, **111**, 68–73.
15 T. W. Hansen and J. B. Wagner, *ACS Catal.*, 2014, **4**, 1673–1685.
16 H. Yoshida, Y. Kuwauchi, J. R. Jinschek, K. Sun, S. Tanaka, M. Kohyama, S. Shimada, M. Haruta and S. Takeda, *Science*, 2012, **335**, 317–319.
17 M. Cabié, S. Giorgio, C. Henry, M. R. Axet, K. Philippot and B. Chaudret, *J. Phys. Chem. C*, 2010, **114**, 2160–2163.
18 H. Frey, A. Beck, X. Huang, J. A. van Bokhoven and M.-G. Willinger, *Science*, 2022, **376**, 982–987.
19 A. S. Almithn and D. D. Hibbitts, *AIChE J.*, 2018, **64**, 3109–3120.
20 Y. Ji, A. M. van der Eerden, V. Koot, P. J. Kooyman, J. D. Meeldijk, B. M. Weckhuysen and D. C. Koningsberger, *J. Catal.*, 2005, **234**, 376–384.
21 S. I. Sanchez, L. D. Menard, A. Bram, J. H. Kang, M. W. Small, R. G. Nuzzo and A. I. Frenkel, *J. Am. Chem. Soc.*, 2009, **131**, 7040–7054.
22 J. H. Kang, L. D. Menard, R. G. Nuzzo and A. I. Frenkel, *J. Am. Chem. Soc.*, 2006, **128**, 12068–12069.
23 B. Roldan Cuenya, A. I. Frenkel, S. Mostafa, F. Behafarid, J. R. Croy, L. K. Ono and Q. Wang, *Phys. Rev. B:Condens. Matter Mater. Phys.*, 2010, **82**, 155450.
24 B. Roldan Cuenya, M. Alcántara Ortigoza, L. K. Ono, F. Behafarid, S. Mostafa, J. R. Croy, K. Paredis, G. Shafai, T. S. Rahman, L. Li, Z. Zhang and J. C. Yang, *Phys. Rev. B:Condens. Matter Mater. Phys.*, 2011, **84**, 245438.
25 J. Timoshenko, M. Ahmadi and B. Roldan Cuenya, *J. Phys. Chem. C*, 2019, **123**, 20594–20604.
26 G. Sun, A. N. Alexandrova and P. Sautet, *J. Chem. Phys.*, 2019, **151**, 194703.
27 C. Mager-Maury, G. Bonnard, C. Chizallet, P. Sautet and P. Raybaud, *ChemCatChem*, 2011, **3**, 200–207.
28 F. Vila, J. Rehr, J. Kas, R. Nuzzo and A. Frenkel, *Phys. Rev. B:Condens. Matter Mater. Phys.*, 2008, **78**, 121404.
29 D. J. Wales, *Annu. Rev. Phys. Chem.*, 2018, **69**, 401–425.

30 M. Bowker, D. James, P. Stone, R. Bennett, N. Perkins, L. Millard, J. Greaves and A. Dickinson, *J. Catal.*, 2003, **217**, 427–433.
31 M. Machida, Y. Uchida, S. Iwashita, H. Yoshida, M. Tsushida, J. Ohyama, Y. Nagao, Y. Endo and T. Wakabayashi, *ACS Catal.*, 2021, **11**, 9462–9470.
32 H. Mistry, F. Behafarid, S. R. Bare and B. Roldan Cuenya, *ChemCatChem*, 2014, **6**, 348–352.
33 F. Behafarid, L. Ono, S. Mostafa, J. Croy, G. Shafai, S. Hong, T. Rahman, S. R. Bare and B. R. Cuenya, *Phys. Chem. Chem. Phys.*, 2012, **14**, 11766–11779.
34 Z. Wei, A. M. Karim, Y. Li, D. L. King and Y. Wang, *J. Catal.*, 2015, **322**, 49–59.
35 Y. Lei, J. Jelic, L. C. Nitsche, R. Meyer and J. T. Miller, *Top. Catal.*, 2011, **54**, 334–348.
36 J. Jones, H. Xiong, A. T. DeLaRiva, E. J. Peterson, H. Pham, S. R. Challa, G. Qi, S. Oh, M. H. Wiebenga, X. I. Pereira Hernández, *et al.*, *Science*, 2016, **353**, 150–154.
37 M. Moliner, J. E. Gabay, C. E. Kliewer, R. T. Carr, J. Guzman, G. L. Casty, P. Serna and A. Corma, *J. Am. Chem. Soc.*, 2016, **138**, 15743–15750.
38 P. Eisenberger and G. S. Brown, *Solid State Commun.*, 1979, **29**, 481–484.
39 B. S. Clausen, H. Topsøe, L. B. Hansen, P. Stoltze and J. K. Nørskov, *Jpn. J. Appl. Phys.*, 1993, **32**, 95.
40 B. Clausena, H. Topsøe, L. Hansen, P. Stoltze and J. Nørskov, *Catal. Today*, 1994, **21**, 49–55.
41 S. T. Chill, R. M. Anderson, D. F. Yancey, A. I. Frenkel, R. M. Crooks and G. Henkelman, *ACS Nano*, 2015, **9**, 4036–4042.
42 A. I. Frenkel, C. W. Hills and R. G. Nuzzo, *J. Phys. Chem. B*, 2001, **105**, 12689–12703.
43 A. M. Karim, V. Prasad, G. Mpourmpakis, W. W. Lonergan, A. I. Frenkel, J. G. Chen and D. G. Vlachos, *J. Am. Chem. Soc.*, 2009, **131**, 12230–12239.
44 G. Dalba, P. Fornasini, R. Grisenti and J. Purans, *Phys. Rev. Lett.*, 1999, **82**, 4240–4243.
45 M. J. Mees, G. Pourtois, E. C. Neyts, B. J. Thijsse and A. Stesmans, *Phys. Rev. B*, 2012, **85**, 134301.
46 R. Wischert, P. Laurent, C. Copéret, F. Delbecq and P. Sautet, *J. Am. Chem. Soc.*, 2012, **134**, 14430–14449.
47 J. Timoshenko, D. Lu, Y. Lin and A. I. Frenkel, *J. Phys. Chem. Lett.*, 2017, **8**, 5091–5098.